Utilization of entrainment for a gravity based recovery of ultrafine particles

Dewes, Ruben M.; Bor, Britta; Rohde, Martin

DOI
10.1016/j.mineng.2025.109520

Publication date
2025

Document Version
Final published version

Published in
Minerals Engineering

Minerals Engineering 232 (2025) 109520

Contents lists available at ScienceDirect

Minerals Engineering

journal homepage: www.elsevier.com/locate/mineng

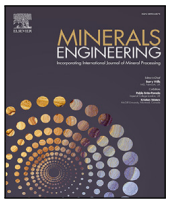

Utilization of entrainment for a gravity based recovery of ultrafine particles

Ruben M. Dewes *, Britta Bor, Martin Rohde

Reactor Institute Delft, TU Delft, Mekelweg 15, 2629 JB Delft, The Netherlands

ARTICLE INFO

Keywords:
Particle recovery
Entrainment
Ultrafine particles
Flow characterization

ABSTRACT

Ultrafine particle recovery poses a complicated challenge to be solved, due to the low collision efficiency with bubbles in flotation processes and a high recovery of gangue material by entrainment. As a result, losses of valuable metals occur. In the present work, a novel approach was chosen for the recovery of ultrafine particles. Instead of flotation, entrainment was used for a gravity based particle recovery. A 3D-printed particle collector was designed to recover the particles at the top of a bubble column. To obtain a good understanding about the density dependence of the process, SiO_2, Ni and W particles were used to cover a density range of 2.65-19.28 g·cm^{-3}. High recoveries were achieved for Ni (73 %) and W (59 %) particles. SiO_2 was only recovered in high amounts (≈50 %) when particle sizes exceeded 10 μm. An extensive investigation of the flow regime was performed to gain an overview about the correlation in between flow regime and particle recovery results.

1. Introduction

Particle recovery from suspension via air bubbling or so called flotation is a widely investigated topic, which finds application in fields like mining industry for mineral valorization, in waste water treatment for impurity removal or in potential future molten salt reactors for fission product removal (Sarrot et al., 2007; Wang and Liu, 2021; Frederix, 2022). The fundamental principle behind flotation is the collision of a hydrophobic particle with a bubble, following its attachment to the bubble and finally its transport out of the flotation cell (Tao, 2005). Mostly, flotation is efficient for a particle range in between 10-100 μm (Trahar and Warren, 1976). For smaller particles, the collection efficiency E_{col} drops rapidly, which is defined as (Hewitt et al., 1995)

$$E_{col} = E_c \cdot E_a \cdot E_s \tag{1}$$

Here, E_c is the collision efficiency, E_a is the attachment efficiency and E_s the stability efficiency. By the definition of the collision efficiency given by Schulze (Schulze, 1989), defined as

$$E_c = E_{ic} + E_g + \left(1 - \frac{E_{ic}}{(1+(d_p/d_b))^2}\right) E_{in} \tag{2}$$

it becomes evident that the collision efficiency highly depends on the ratio between particle and bubble size. Here, E_{ic} is the interception effect, E_g the gravitational effect, E_{in} the inertial effects, d_p the particle diameter and d_b the bubble diameter. In this context, both, the inertial effect and gravitational effect play a significant role, where both decrease with decreasing particle size and thus, reducing the overall collision efficiency. The gravitational effect is defined as

$$E_g = (1+(d_p/d_b))^2 \frac{v_S^*}{1+v_S^*} sin^2\Theta_c \tag{3}$$

and the inertial effect as

$$E_{in} = \frac{1}{1+v_S^*}(1+(d_p/d_b))^2 \left(\frac{St}{St+a}\right)^b \tag{4}$$

where v_S^* is the ratio of the particle settling velocity and bubble rise velocity v_{ps}/v_b, Θ_c a parameter depending on the bubble Reynolds number Re_b, a and b constants depending on Re_b and St the Stokes number. Especially for extremely fine particles, the collision efficiency becomes small and the recovery unlikely. An option to improve the collision efficiency is to reduce the bubble size. However, a reduction of bubble size comes with drawbacks for the flotation process, namely, low bubble rise velocity and lifting force. As a result, fully loaded bubbles might not provide sufficient lift to transport the particles to the top or in general long flotation times are required (Farrokhpay et al., 2020; Miettinen et al., 2010).

A phenomenon that is occurring simultaneously in the flotation process is entrainment, which is described as a mechanical mass transfer process of particles in a flotation cell. In literature, three theories are established which describe the different processes which can cause entrainment. According to the Boundary Layer Theory, particles can be transported in the hydrodynamic layer of water surrounding the bubble. Another transport possibility, according to the Bubble Wake

* Corresponding author.
E-mail addresses: r.m.dewes@tudelft.nl (R.M. Dewes), m.rohde@tudelft.nl (M. Rohde).

https://doi.org/10.1016/j.mineng.2025.109520
Received 3 February 2025; Received in revised form 7 June 2025; Accepted 8 June 2025
Available online 27 June 2025

Theory, is the transport of particles in the wake of bubbles. The third theory is the Bubble Swarm Theory, where entrainment is occurring, due to bubbles pushing particles up to the froth and building a layer after layer where particles are getting entrapped (Wang et al., 2015). Entrainment is seen as an unwanted phenomenon, as it is not transporting particles selectively, which leads to the recovery of impurities (Neethling and Cilliers, 2009). However, entrainment is rather efficient at transporting ultrafine particles, as these tend to follow the streamlines of the bubbles (Leistner et al., 2017). In the here presented study it is investigated, if entrainment can be used to selectively recover ultrafine particles. For this purpose, a 3D-printed particle collector was designed and tested for its suitability for density (2.65 g·cm^{-3} – 19.25 g·cm^{-3}) and size based (500 nm – 10 μm) particle recovery. From bubble size and frequency measurements, correlations between the bubble regime and particle recovery were drawn.

2. Materials & methods

2.1. Materials

Particles for the experiments were obtained from US Research Nanomaterials Inc. A particle size of 500 nm, 1 μm, 5 μm and 10 μm was purchased for Ni (99.5% , ρ = 8.91 g·cm^{-3}). Due to limited supply, only particle sizes of 500 nm, 1 μm and 5 μm were obtained for W (99.9% , ρ = 19.25 g·cm^{-3}). For SiO_2 particles (99.5% , ρ = 2.65 g·cm^{-3}), sizes of 1 μm, 5 μm and 10 μm were used.

2.2. Experimental setup

The experiments were performed in an in-house manufactured PMMA-column, as depicted in Fig. 1. In total, the height of the column is 450 mm with an inner diameter of 30 mm. To allow accurate optical measurements, the front of the column is milled to remove the curvature and thus, minimizing distortion. Both, at the bottom and top of the column, flanges are attached to allow a facile installation of gas inlet and particle collector. The gas inlet has a diameter of 1 mm, which turns into a conical shape of an angle of 45° that ends at the column wall. Air flow regulation was achieved by a Bronkhorst EL-Flow Select flow controller with an accuracy of 0.5%, which can provide volume flows in between 5–500 cm^3·min^{-1}.

The particle collector is a specially designed 3D-print with a total length of 100 mm. It takes advantage of the entrainment of particles in the bubble wake, and can be inserted at the top of the column. In the center, a conical opening with a diameter of either 7.5 or 10 mm is located, where bubbles passing through transport the particles to the collector, after which they sediment and can be removed. The height of the cone is 10 mm, leading to a cone angle of 60 or 64.3°. A schematic representation of the separation principle is shown in Fig. 2.

2.3. Methodology

At the beginning of the experiments, the gas flow was set in between 150–450 cm^3·min^{-1}, after which the column was filled with demineralized water. Following this, the particles were added with a mass of 0.1 g for SiO_2 and 0.2 g for Ni and W. The difference in weight was chosen to not obtain a too high particle concentration for potential optical-measurements. After the particles were dispersed sufficiently by the bubble flow, the particle collector was inserted and the column was filled up to the final liquid level. In total, a separation time of 60 min was chosen to guarantee a steady-state, which represents the maximal possible recovery. At the end of the experiment, the gas flow was turned off and the particle collector was removed carefully from the column. The particles were flushed out of the particle collector over a vacuum filtration setup. As filtration membrane, a Merck Millipore PVDF membrane with a pore size of 0.1 μm was used. After the filtration, the membranes with particles were left drying in air. From the weight difference of the membrane without and with particles, the recovery was calculated. The standard error for the experiments was only determined by 3 repetitions for the Ni-recovery of 500 nm and 10 μm particles at a volume flow of 150 and 350 cm^3·min^{-1}, due to the long experimental time. It is expected that only a methodological error is present and that the material properties themselves do not significantly play a contribution. The maximum standard error measured was 5 %, which indicates good reproducibility of the experiments.

2.4. Characterization

2.4.1. Bubble parameters

For the characterization of the bubble size, a Nikon Z50 was used in combination with a Nikkor MC 105/2.8 S lens. As camera settings, a shutter time of 1/1000 s, an aperture of 5.6 and an ISO-value of 6400 were used. Manually, the images were cropped to obtain separate bubbles. Here, bubbles were discarded which were not in focus or overlapping with other bubbles. The background of the obtained images was removed using macOS Sonoma 14.1.2. Post-processing was performed using Python, where pictures were converted into a grey image. The boundaries of the bubbles were determined by the difference in background intensity. Following, with 50 points in horizontal and 50 points in vertical direction, the outline of the bubble was identified, as shown in Fig. 3. As the bubble regimes present in the column are spherical or spheroidal, it was assumed that an ellipsoidal shape represents the bubble shape sufficiently accurate, and through the obtained points, an ellipsoidal fit was put, using a least squares dogbox method. From the minor and major axis of the fit, the bubble chord length was calculated according to Mohagheghian and Elbing (2018) as follows

$$d_b = \sqrt{\frac{4bA_{proj}}{\pi}} \tag{5}$$

where b is the ratio of the major and minor axis and A_{proj} the cross sectional area of the bubble. In total, a number of at least 94 and maximum of 164 bubbles was used to determine the population and Sauter mean diameter of each investigated volume flow. The uncertainty estimation for the Sauter mean diameter was performed by calculating the standard error.

To determine the bubble frequency, slow motion videos were recorded with the camera equipment and settings mentioned above for a recording period of at least 30 s. The number of bubbles yielded, ranging from 139–1219 bubbles, was large enough to minimize the error of miscounting. For direct comparison, the number of counted bubbles was divided by the recording time to obtain a bubble frequency.

2.4.2. Laser Doppler Anemometry

The device used for Laser Doppler Anemometry (LDA) measurements is a Dantec Dynamics Flowexplorer DPSS, equipped with a dual laser setup with back-scattering type receiver. As measurement region, the center of the height and diameter of the column was chosen, to allow the bubbles to reach terminal velocity and to avoid any effects caused by the proximity of the liquid surface. Measurements consisted of three repetitions with a run time of 3 min each. Processing of the data was performed using MATLAB R2021b. A satisfying description of the curve shape was achieved using a Gaussian fit of the type `gauss2` with an R^2 of at least 0.999.

2.5. Scanning electron microscopy

The analysis of sample morphology was performed using a Joel JSM-IT100 InTouchScope^{TM}. The current used was in between 10–15 kV and no coating was applied, due to the good conductivity of the samples.

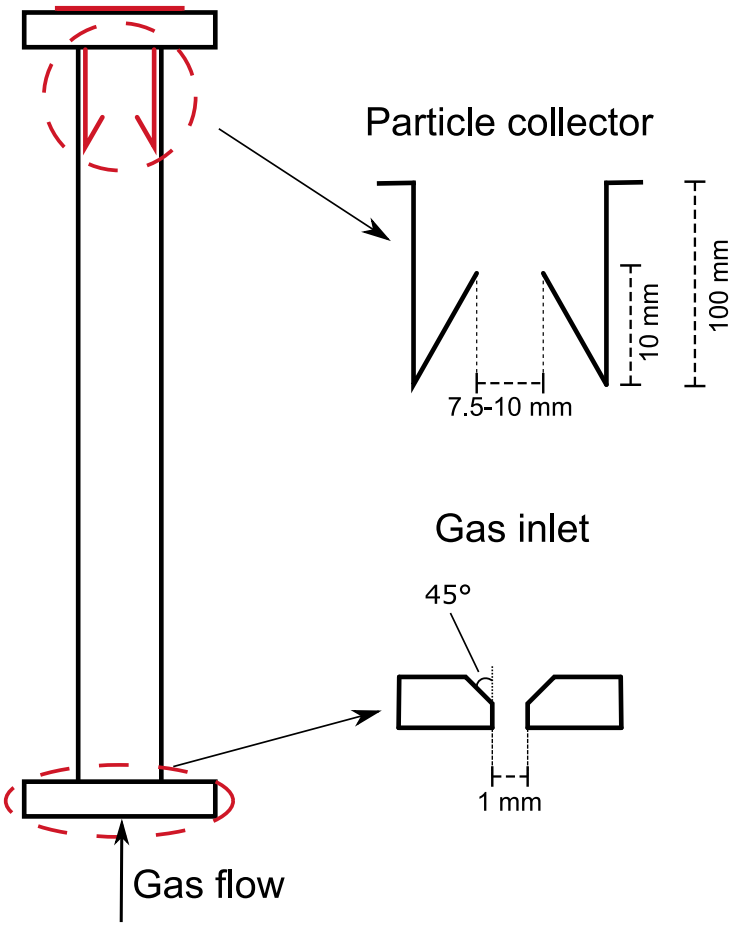

Fig. 1. Experimental setup of the bubble column, including the depiction of the particle collector and gas inlet.

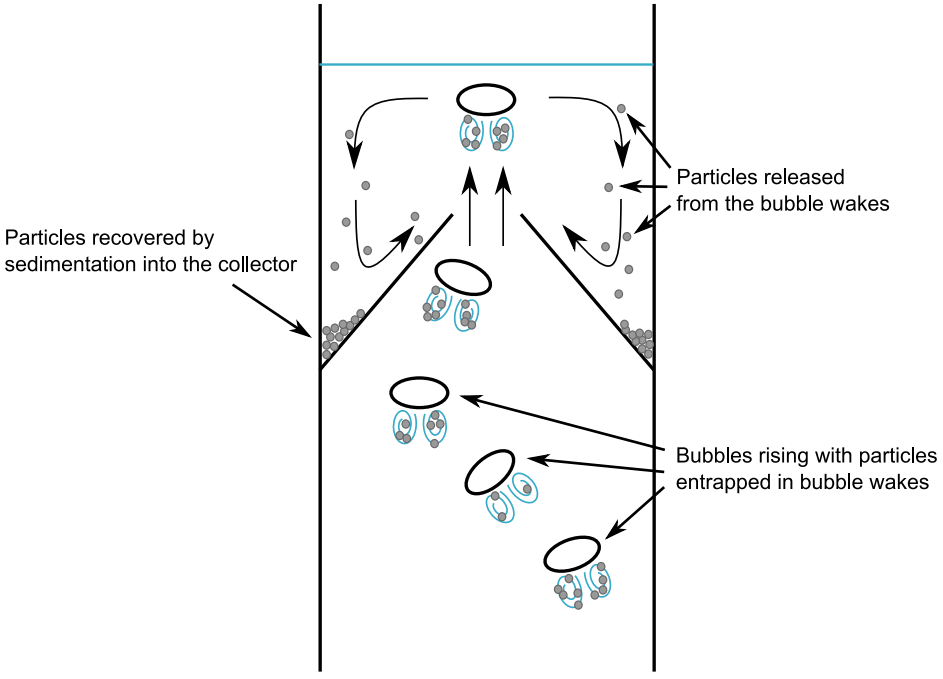

Fig. 2. Separation principle for the recovery of ultrafine particles via entrainment, based on the here presented particle collector.

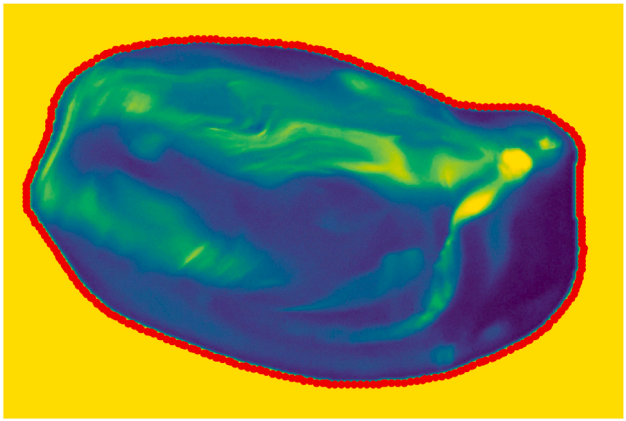

Fig. 3. Detected bubble outline by the used Python code for the determination of the Sauter mean diameter.

3. Results & discussion

3.1. Investigation of bubble regime

As the particle recovery depends highly on the bubble regime, a thorough investigation was performed to understand the changes occurring in the bubble column at different volume flows. In Fig. 4 the change of Sauter mean diameter and bubble frequency are shown. A decrease of Sauter mean diameter from 10 mm to 6.7 mm is observed for volume flows until 100 $cm^3 \cdot min^{-1}$, after which a constant increase follows to nearly 15 mm. At low volume flows, the flow meter is not able to provide a constant air flow, due to reduced metering accuracy close to the minimal volume flow. This leads to short bursts of air, which produce relatively large bubbles. With increasing volume flow, the metering accuracy improves and a constant bubble flow is reached at around 100 $cm^3 \cdot min^{-1}$. Consequently, the smallest Sauter mean diameter is measured under these conditions. When the volume flow is increased to higher flow rates than 100 $cm^3 \cdot min$, the bubbles start to grow larger in size, on the expense of number of bubbles being present in the column, as can be seen from the bubble frequency. It appears that a change from the homogeneous to the transitional bubble regime occurs under these bubbling conditions. This trend continues until a volume flow of 200 $cm^3 \cdot min^{-1}$ is reached. Especially at 300 $cm^3 \cdot min^{-1}$ a jump both, in Sauter mean diameter and bubble frequency is observed, indicating the change to the heterogeneous bubble regime. The here determined relatively large Sauter mean diameter of more than 10 mm gives an insight into the transport process affecting the particles. As the bubble size is significantly larger than the particle size ($d_p \ll d_B$), it follows that according to Eq. (2), the collision efficiency converges towards zero. Consequently, it can be assumed that the dominant transport process in the bubble column is entrainment.

A comparable behavior can be observed for the number distribution of the bubbles, as shown in Fig. 5. Here, the number distribution becomes narrower towards a volume flow of 100 $cm^3 \cdot min^{-1}$, showing again the metering difficulties of the flow meter at low volume flows. The sharp peaks noticeable at 75 and 100 $cm^3 \cdot min^{-1}$ are characteristic for the homogeneous bubble regime, where only small deviations are present in bubble size. Within the range of 150–250 $cm^3 \cdot min^{-1}$, the number distribution of the bubbles shifts to a larger bubble diameter and broadens slightly. However, no significant difference is present in between each of the distributions in this range. Further increase of the volume flow leads to a significant broadening of the number distribution. Thus, confirming the visually observed presence of intense bubble coalescence and break-up, which is characteristic for heterogeneous or also so called churn turbulent flows (Montoya et al., 2016).

As a result of the changes in bubble regime, the liquid flow patterns within the column change at different volume flows, consequently. With LDA-measurements and neutrally buoyant glass hollow spheres, the vertical velocity distribution locally present in the column can be determined and the corresponding full width at half maximum (FWHM), as shown in Fig. 6. In accordance with the identification of the bubble regimes above, the velocity distribution in the bubble column changes comparably. Under the conditions where a homogeneous regime is present, a narrow velocity distribution occurs, due to the small and evenly distributed bubble size. With the onset of the transitional regime, the velocity distributions start to widen significantly. The increase of bubble size leads to a higher bubble rise velocity and thus, generally higher velocities are reached in the column. Through further increase of the volume flow, the velocity distributions keep on widening until around 350 $cm^3 \cdot min^{-1}$. Here, two phenomena are mainly limiting a further increase of flow velocity in the column. On one hand, the bubble breakup in the heterogeneous flow regime limits the maximum bubble size reached. As a result, the bubbles present do not experience as much buoyancy. On the other hand, if the bubbles are not experiencing breakup, they reach a size where the bubbles are close to create some sort of slug flow. Due to the interactions with the wall, the bubbles are getting slowed down and again, a limitation of bubble rise velocity is caused.

3.2. Particle recovery via entrainment

A wide range of densities (2.65–19.28 $g \cdot cm^{-3}$) is investigated to obtain a general overview of the density dependence of the here proposed process. Here, SiO_2 is supposed to represent gangue material, due to its low density. For the recovery of SiO_2 no significant difference in recovery can be observed depending on the opening diameter of the particle collector, as shown in Fig. 7. Additionally, the volume flow appears to have no effect on the recovery of SiO_2 as well. The low sedimentation velocity and inertia resulting from the low density and size keep the particles afloat, regardless of the gas volume fraction present in the bubble column. On the contrary, the particle size appears to have a strong effect on the SiO_2 recovery. A gradual increase can be observed with increasing particle size. With a particle size of 1 μm only a recovery of roughly 10 % is achieved, increasing to nearly 30 % for 5 μm particles and reaching a maximum for the 10 μm particles at around 50 %. It appears that especially the combination of low density and small particle size prevents the recovery of SiO_2 particles. In the process introduced here, the separation is based on the sedimentation of particles on the top of the column into the particle collector. For particles around 1 μm, the sedimentation velocity is too small to allow a recovery in the process here introduced. The forces that the particles are experiencing by the liquid movement of the passing bubbles are larger than the gravitational force. Consequently, the particles stay afloat and cannot be recovered. The terminal sedimentation velocity of the particles increases quadratically with the particle radius, according to equilibrium of the drag force described by Stokes' law ($F_d = 6\pi\mu R v$) and the interplay of gravitational and lift force described by the Archimedes' principle ($F_a = (\rho_p - \rho_f) g V_p$). At small particle size, in combination with low density, the threshold for recovery is not fulfilled for the SiO_2 particles. The sedimentation velocity of the particles is not large enough for the particles to settle at the bottom of the collector. Due to the low terminal sedimentation velocity, it is more likely for the particles to get entrapped in the velocity fields present in the collector. As a result, particles might rather leave the collector again and enter the column, instead of being recovered. In comparison, an increase of sedimentation velocity of up to 100 times occurs for the 10 μm particles. This appears to increase the number of particles, for which the threshold for recovery is fulfilled significantly.

A qualitative overview about the particle size was obtained by SEM, as shown in Fig. 8. As expected, the particles present in the 1 μm SiO_2 sample show overall a small particle size. However, occasional larger

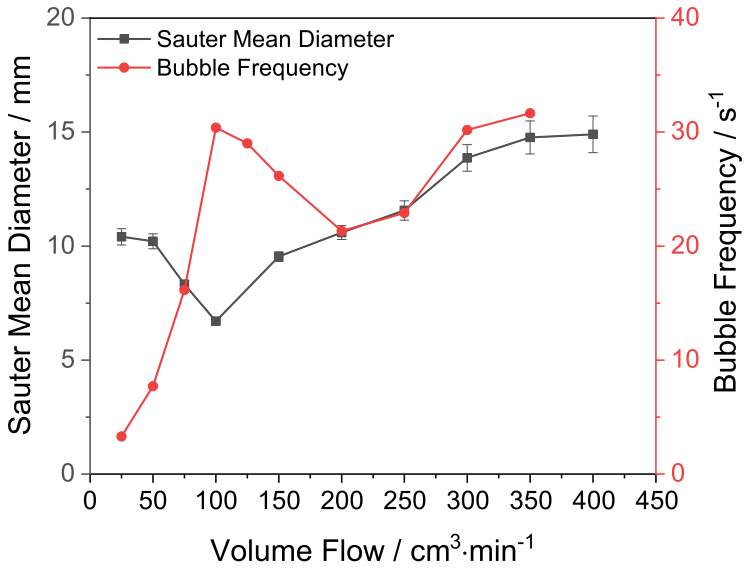

Fig. 4. Sauter mean diameter (black line, squares) and bubble frequency (red line, circles) for different volume flows (25–400 $cm^3 \cdot min^{-1}$) used in the bubble column. (For interpretation of the references to color in this figure legend, the reader is referred to the web version of this article.)

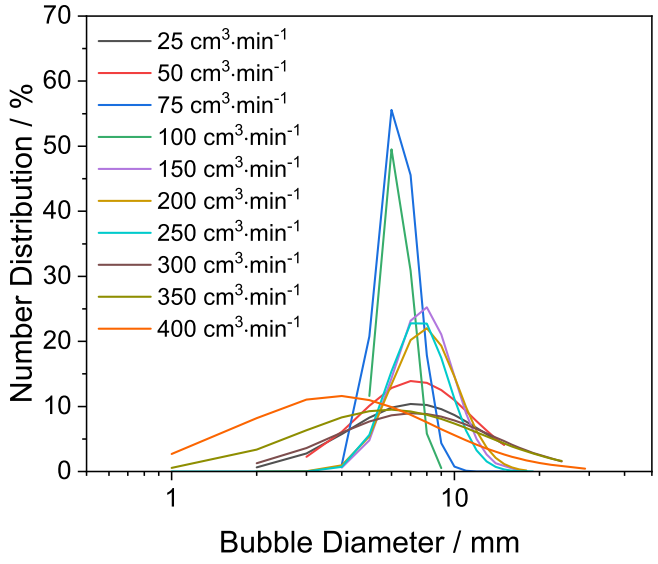

Fig. 5. Number distribution of the determined bubble diameters at volume flows ranging from 25–400 $cm^3 \cdot min^{-1}$.

particles are observed in the particle size range of approximately 10 μm. The fraction of larger particles in the sample appear to correlate to the percentage of SiO_2 recovered. Hence, underlining the assumption that the sedimentation velocity is the recovery limiting step for small SiO_2 particles. As expected, larger particles are observed in the 5 μm sample. Overall, the percentage of particles above 10 μm present increased, which is in good accordance with the observed increased of particle recovery. In the 10 μm SiO_2 sample, a large increase of particle size is observed, reaching sizes of up to 30-40 μm. Here, not only entrainment plays a role in the particle lift, but the general flotation process can contribute to the particle transport to the top of the column as well. According to Eq. (2), the collision efficiency increases quadratically with the particle size. Thus, a significant increase in particle collisions with the bubbles is expected. Consequently, the efficiency of the SiO_2 recovery increases further. Another effect influencing the recovery of SiO_2 is the shape of the particles. In comparison with the other particles investigated, SiO_2 is the only sample not showing a spherical morphology. Research performed by Wiese et al. (2015) showed that the entrainment of particles is affected by their shape. Especially non-spherical particles experienced a higher degree of entrainment. As a result, a higher degree of entrainment is expected for the SiO_2, in comparison to the other particles used in the here presented study. Thus, the recovery of SiO_2 is partly overestimated in comparison to the spherical samples presented below.

The recovery of Ni-particles for the 7.5 mm and 10 mm particle collector is shown in Fig. 9. For the 7.5 mm particle collector, for all particles an increase in recovery occurs with increasing volume flow until 350 $cm^3 \cdot min^{-1}$. The maximum recovery for the 10 μm Ni-particles reaches up here to 62 %, 73 % for 5 μm, 67 % for 1 μm and 58 % for 500 nm. At lower flow rates, the bubbles are not large enough to generate sufficient lift in their wakes for especially larger particles. Additionally, the lower bubble frequency at lower volume flows leads to a generally low number of upwards transport events. Thus, the bubble regime present is not able to prevent sedimentation from occurring. The stagnating recovery from 200–250 $cm^3 \cdot min^{-1}$ of the 5 and 10 μm is also attributed to this limitation. Right at the boundary between transitional and heterogeneous bubble regime, no significant difference in bubble frequency is present. However, the bubble size keeps on increasing and with it the lift generated by the bubbles. Thus, bubble sizes above 10 mm should generate sufficient lift for the here presented recovery process for Ni-particles up to 10 μm. The relatively low number of bubbles at these volume flows is not sufficient to keep all the particles dispersed. Consequently, particles are lost due to sedimentation. With entering the heterogeneous bubble regime, the bubble frequency starts rising again and with it sedimentation is reduced. As a result, recovery rises with increasing volume flow again. At a volume flow of 400 $cm^3 \cdot min^{-1}$ a sudden drop in recovery can be observed for all cases. Here, the gas volume injected into the bubble column is too large to easily pass through the restriction of the particle collector. An air pocket forms right underneath the opening of the bubble collector. When the air volume held underneath the particle collector reaches a critical point, the buoyancy of the air forces the pocket through the hole and a new air pocket begins forming. Only during these sudden lift moments, it is possible for particles to move in between bubble column and particle collector. Thus, a reduced recovery is present. For the 500 nm a comparable recovery trend can be observed as for the 5 and 10 μm particles. Due to the smaller size, the maximum recovery for the 500 nm Ni-particles is lower. As the recovery in the particle collector is based on particle sedimentation,

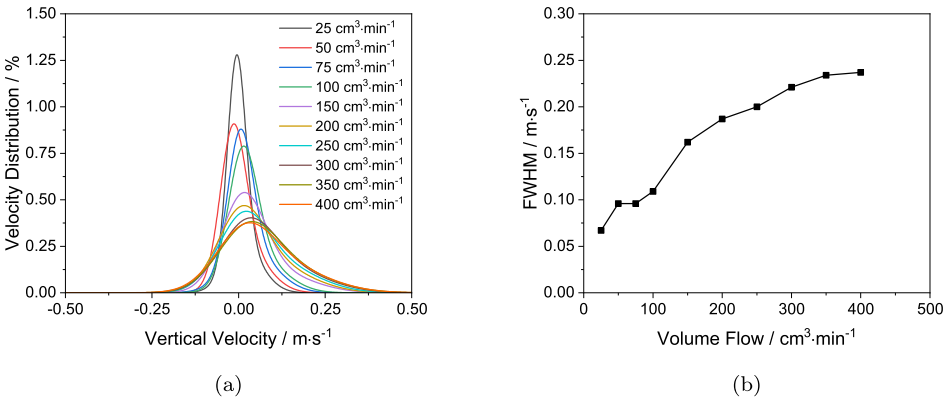

Fig. 6. Velocity distributions measured by LDA for neutrally buoyant glass beads in a volume flow range in between 25–400 $cm^3 \cdot min^{-1}$ (a) and the corresponding FWHM (b).

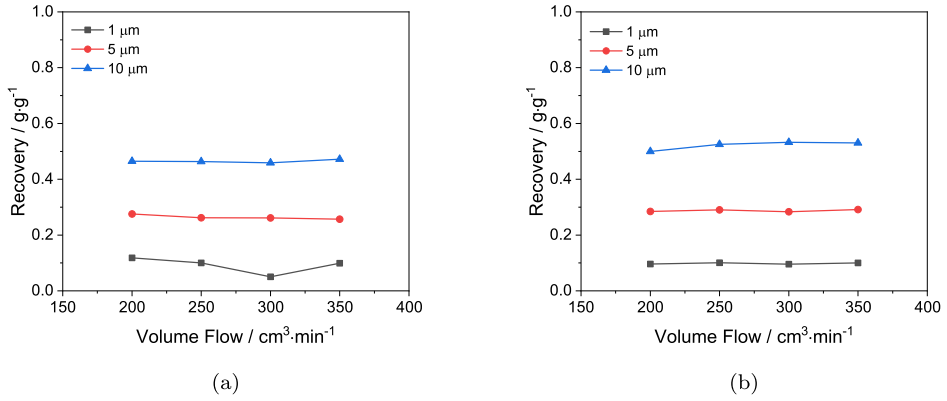

Fig. 7. Recovery of SiO_2 particles for a particle size of 1 µm (black line, squares), 5 µm (red line, circles) and 10 µm (blue line, triangles up) for a particle collector with an opening diameter of 7.5 mm (a) and 10 mm (b), with an estimated maximum standard error of 5 %. (For interpretation of the references to color in this figure legend, the reader is referred to the web version of this article.)

the low sedimentation velocity of the small particles inhibits particle settlement. The bubbles passing through the opening create a flow field strong enough to keep the smaller particles dispersed in the water. As a result, these particles can exit the particle collector again to re-enter the bubble column section.

For the particle collector with an opening diameter of 10 mm, a comparable recovery trend to the one of 7.5 mm can be observed for the 5 and 10 µm Ni-particles. The recovery increases until a maximum of 350 $cm^3 \cdot min^{-1}$. However, only a recovery of 59 % is achieved for the 5 µm particles and 54 % for the 10 µm particles. The particle collector with an opening diameter of 10 mm underperforms here, due to two phenomena. On the one hand, there is less area available where particles can sediment. On the other hand, the wider opening allows the bubbles to pass through with a higher bubble rise velocity. Particles are rather flushed out of the particle collector than being allowed to sediment. This can be seen by the recovery drop for both 5 and 10 µm at 400 $cm^3 \cdot min^{-1}$. Especially for the 500 nm particles, this flushing out can be observed. The recovery maximum is present at 250 $cm^3 \cdot min^{-1}$ with 55 %. The more intense velocity field in the particle collector, caused by the higher bubble rise velocity, leads to a strong flushing out of the small particles. With increasing volume flow, the recovery drops consequently.

For the Ni-particles of 1 µm a generally high recovery is observed for both particle collectors. Characteristic trends can be observed like a recovery drop at the boundary between transitional and heterogeneous bubble regime, as well as a flushing out for the 10 mm particle collector. However, the recovery would be expected to lay somewhere in between the trend of the 500 nm and 5 µm particles. Yet, a generally high recover is obtained under most of the conditions. To obtain more insight, SEM-images were taken of the samples, which are shown in Fig. 10. It can be seen that the 500 nm, 5 µm and 10 µm particles are possessing a spherical shape, as indicated by the supplier. On the contrary, the 1 µm particles seem to have sharp edges and appear to be intergrown. Long Ni-chains seem to have formed with large cavities in between them. The combination of the formation of larger, but hollow particle structures, seem to be beneficial for the here presented recovery technique.

In comparison with results reported in literature, the here presented technique shows a higher recovery for ultrafine Ni-particles. Wang et al. (2024b) were only able to achieve a Ni-recovery of 10–15 % for sub 20 µm Ni-particles, despite proving a generally high recovery in their overall flotation process. In another study (Wang et al., 2024a), recoveries of around 60 % are reported for Ni-particles below 20 µm, which is nearly as high as the results reported here. However, the research in Wang et al. (2024b,a) was performed using actual mineral compositions, whereas the research presented here investigated pure materials. Consequently, a direct comparison must be critically taken into account.

In Fig. 11, the recovery of W is shown for a particle collector with an opening diameter of 7.5 and 10 mm. For the 7.5 mm particle collector, the 5 µm particles seem to increase in recovery with increasing volume flow and reach a maximum recovery at 300 $cm^3 \cdot min^{-1}$ with 45 %. No significant difference is observed at higher volume flows. The W-recovery is rather low, as the narrow opening diameter of 7.5 mm leads to a reduction of the bubble rise velocity when the bubbles are passing through. Due to the high density of W, the low bubble rise velocity during the passage through the narrow particle collector opening is not sufficient enough to sustain the upwards movement of the W-particles. As a result, only a limited number of particles enters the particle collector. For the 10 mm particle collector, generally higher recoveries

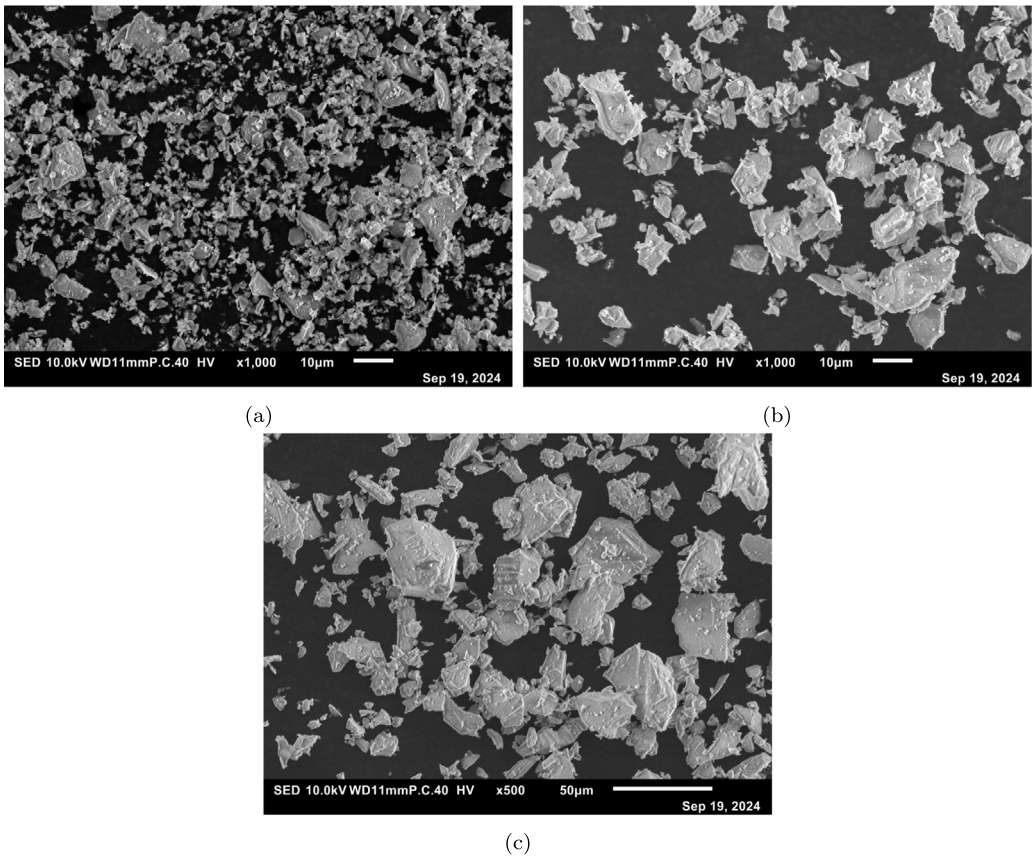

Fig. 8. SEM images of received SiO_2 samples with a particle size of 1 µm (a), 5 µm (b) and 10 µm (c).

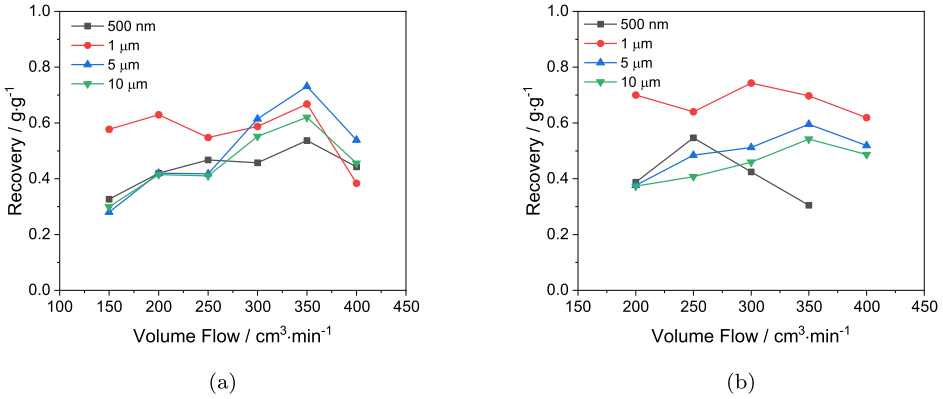

Fig. 9. Recovery of Ni particles for a particle size of 500 nm (black line, squares), 1 µm (red line, circles) and 5 µm (blue line, triangles up) and 10 µm (green line, triangles down) for a particle collector with an opening diameter of 7.5 mm (a) and 10 mm (b), with an estimated maximum standard error of 5 %. (For interpretation of the references to color in this figure legend, the reader is referred to the web version of this article.)

are achieved than for the 7.5 mm particle collector. Surprisingly, two maxima can be observed for the 5 µm W-particles. One is located at 250 $cm^3 \cdot min^{-1}$ with 53 % and the other one at 450 $cm^3 \cdot min^{-1}$ with 59 %. Additionally, a local minimum is also present at 350 $cm^3 \cdot min^{-1}$ with 43 %. Through the high density of W, larger bubbles are beneficial for a stronger entrainment of the particles. Until 250 $cm^3 \cdot min^{-1}$, the bubble size continuously increases in the transitional bubble regime, leading to an increase of generated bubble lift. At the onset of the heterogeneous bubble regime at 300 $cm^3 \cdot min^{-1}$, the general Sauter mean diameter still keeps on increasing. However, the bubble regime is experiencing constant bubble coalescence and bubble break up, leading to a wide bubble size distribution, as discussed before in Fig. 5. The smaller bubbles formed during the bubble break up are not large enough to lift the W-particles efficiently, whereas the larger bubbles formed by coalescence are not represented sufficiently in number. Thus, a drop in recovery occurs until the minimum at 350 $cm^3 \cdot min^{-1}$. With further increasing volume flow, the number of larger bubbles increases as well and the recovery starts rising from 400 $cm^3 \cdot min^{-1}$ onwards. The reported maximum recovery of the 5 µm W-particles is not necessarily the highest achievable recovery. Due to the operating limitations of the flow meter, higher volume flows were not investigated. For both, the 500 nm and 1 µm W-particles, it appears that the volume flow does not have a significant effect on the recovery. However, the recovery for the 10 mm particle collector is around 10 % higher than the 7.5 mm particle collector. Investigating the samples with a SEM uncovers that large agglomerates in the shape of cubicles are present in the 500 nm

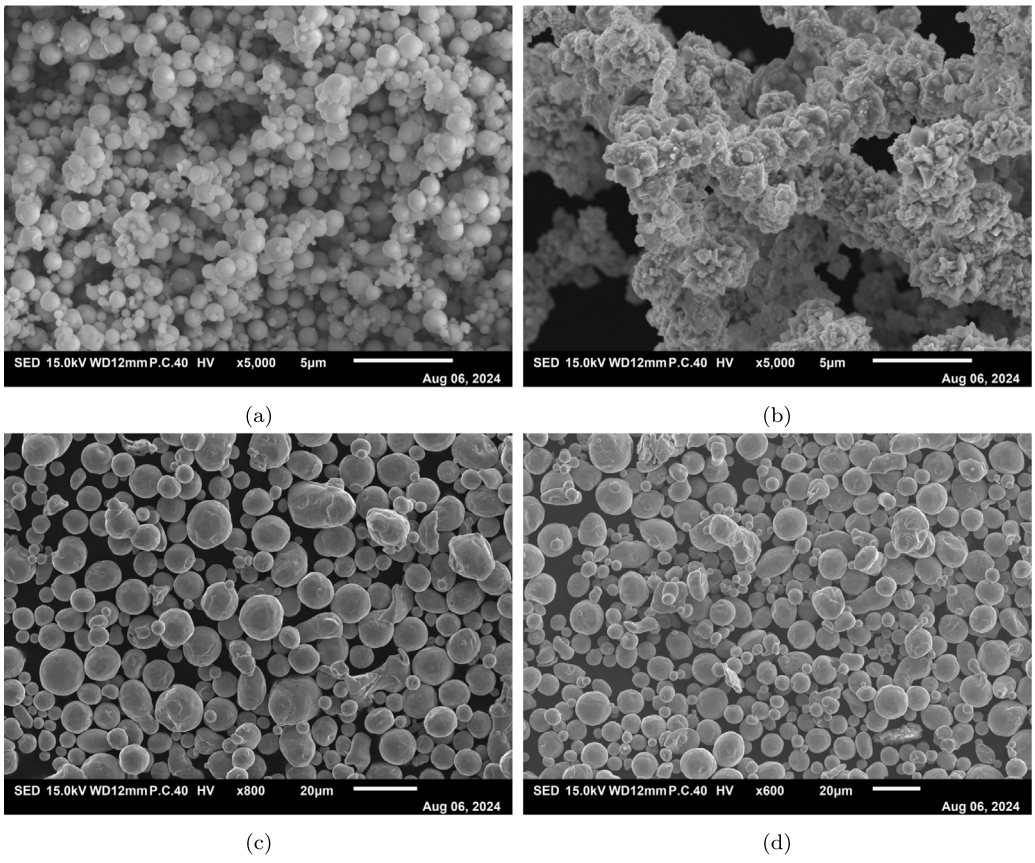

Fig. 10. SEM images of received Ni samples with a particle size of 500 nm (a), 1 µm (b), 5 µm (c) and 10 µm (d).

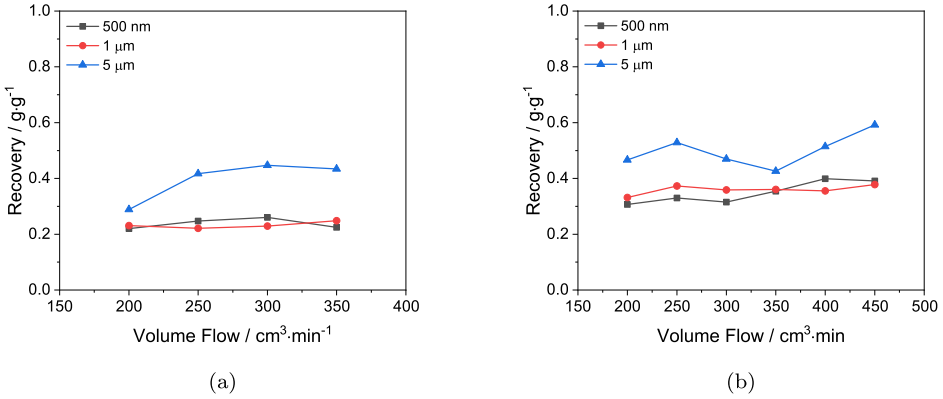

Fig. 11. Recovery of W particles for a particle size of 500 nm (black line, squares), 1 µm (red line, circles) and 5 µm (blue line, triangles up) for a particle collector with an opening diameter of 7.5 mm (a) and 10 mm (b), with an estimated maximum standard error of 5 %. (For interpretation of the references to color in this figure legend, the reader is referred to the web version of this article.)

and 1 µm samples, as shown in Fig. 12. The cubicles are around 50 µm in size and take over a significant fraction of the samples. Agglomerates of this size are too heavy to be lifted in the bubble wakes. Therefore, only low recoveries are achieved for the 500 nm and 1 µm samples.

Overall, the recovery obtained here is comparable to alternatives reported in literature. Huu Huu Hoang et al. (2022) investigated the recovery of fine gold loss tailings. The similarity in densities in between Au and W allows the direct comparison, due to the process solely relying on a density and size based recovery. Without the usage of reagents, recoveries in between 50–68 % were achieved for particles smaller than 38 µm and 65–68 % with reagents for particles below 20 µm. Under consideration of a gradual decrease of recovery efficiency with decreasing particle size, the here obtained recovery of 59 % for the 5 µm W particles is competitive with the commercial flotation cell.

4. Conclusion

A new separation process for ultrafine particles was introduced in the here presented study. Instead of relying on flotation, the usually avoided entrainment was assessed for feasibility as separation process. For this purpose, a gravity based separation process was developed, using a 3D-printed particle collector at the top of the bubble column. The successful recovery of metal particles was proven for Ni and W. With the here presented methodology, a recovery of Ni-particles of up to 73 % was achieved and 59 % for W-particles. An interplay in

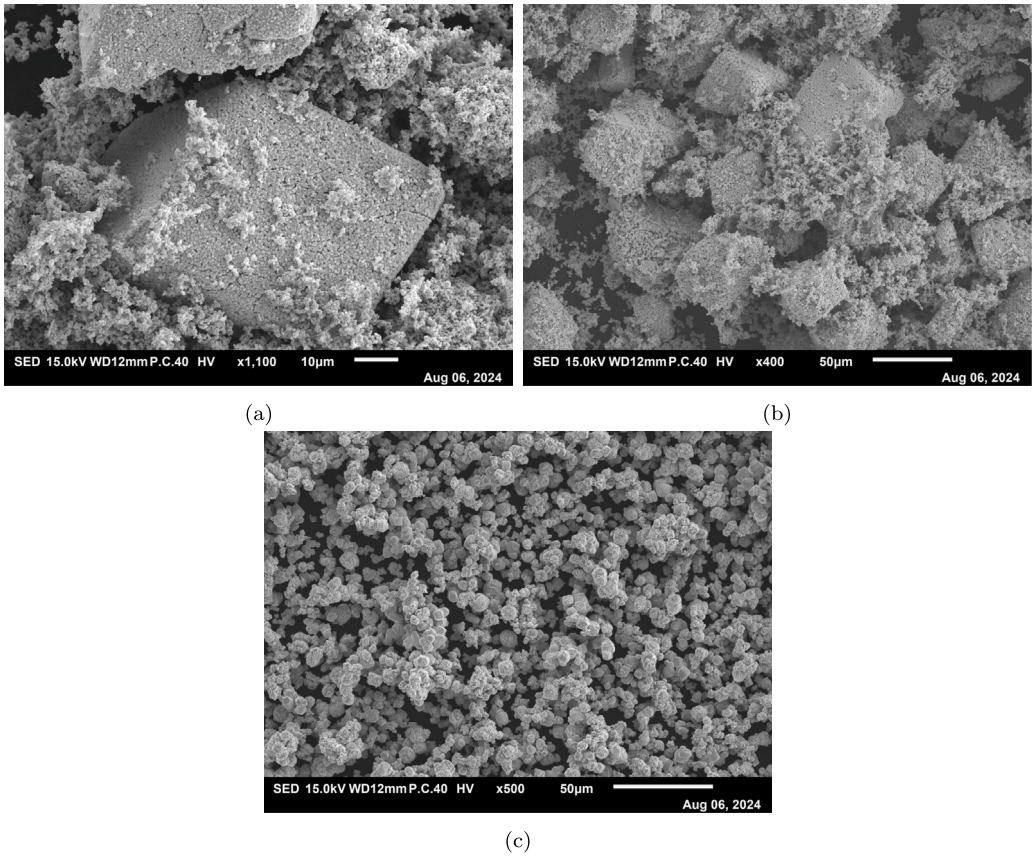

Fig. 12. SEM images of received W samples with a particle size of 500 nm (a), 1 µm (b) and 5 µm (c).

between bubble size, bubble frequency, particle density and size was found, due to an extensive investigation of the bubble regime in the column. Ideally, a turbulent regime is used for Ni-particles with a not too high gas volume fraction in the bubble column. In contrast, for the W-recovery an increasing gas volume fraction seemed to be beneficial. Due to the limitations of the flow meter, ideal operation conditions could not be determined and an optimum is expected to be present beyond the investigated volume flows. In terms of particle collector geometry design, there is a dependence on the recovery efficiency of the particle density. For Ni-particles, an opening diameter of 7.5 mm provides a higher recovery, due to a larger surface area on which the particles can sediment. However, the heavier W-particles benefit from a 10 mm opening diameter. The larger opening diameter allows for the operation at higher volume flows, without the risk of an air pocket forming underneath the particle collector. Thus, a stronger particle lift can be achieved that is required for high densities. The lightest material investigated, namely SiO_2, showed to be not significantly affected by varying volume flow conditions. The recovery in general was low except for particles of larger sizes. Only 10 % of SiO_2 particles were recovered of the 1 µm sample. For the larger sample of 10 µm, a high recovery of 50 % was achieved, due to a large fraction of the sample being of a size significantly larger than 10 µm. Overall, it can be concluded that for light material like SiO_2 the gas volume flow is insignificant for the recovery and the particles cannot be recovered efficiently for particle sizes below 10 µm. However, when a critical size is exceeded, a high recovery is obtained. Larger material densities like Ni and W introduce a dependence on the volume flow. Churn turbulent flows are more beneficial and recovery appears to be reduced for particle sizes below 1 µm.

The strong dependence of recovery on density and size could be exploited in mining processes. It could enable the valorization of ultra-fine particle tailings, where gangue material of similar density to SiO_2 would not be recovered, whereas valuable heavier material is collected on the top of the column. Here, it would be essential to guarantee a sufficient grinding of the tailing, to assure a particle size below 10 µm. Especially the avoidance of surfactants or other chemicals in the process allows a reduction of capital costs and environmental impact. Additionally, application could be found in the currently developed molten salt reactors. During the fission cycle, non-soluble platinoid group particles like Mo-99 are formed. These particles formed obtain a small particle size and well established separation techniques cannot be applied, due to the complexity of the molten salt system. Thus, particle valorization and prevention of particle attachment to the walls could be potentially achieved.

CRediT authorship contribution statement

Ruben M. Dewes: Writing – original draft, Methodology, Investigation, Formal analysis, Data curation, Conceptualization. **Britta Bor:** Methodology, Investigation, Formal analysis, Data curation. **Martin Rohde:** Writing – review & editing, Supervision, Project administration, Funding acquisition, Conceptualization.

Declaration of competing interest

The authors declare the following financial interests/personal relationships which may be considered as potential competing interests: Martin Rohde reports financial support was provided by Euratom Research and Training Programme. If there are other authors, they declare that they have no known competing financial interests or personal relationships that could have appeared to influence the work reported in this paper.

Acknowledgments

The MIMOSA (MultI-recycling strategies of LWR SNF focusing on MOlten SAlt technology) project has received funding from the Euratom Research and Training Programme under grant agreement no. 101061142. Views and opinions expressed are however those of the author(s) only and do not necessarily reflect those of the European Union. Neither the European Union nor the European Commission can be held responsible for them.

Data availability

Data will be made available on request.

References

Farrokhpay, S., Filippova, I., Filippov, L., Picarra, A., Rulyov, N., Fornasiero, D., 2020. Flotation of fine particles in the presence of combined microbubbles and conventional bubbles. Miner. Eng. 155, 106439. http://dx.doi.org/10.1016/j.mineng.2020.106439.

Frederix, E.M.A., 2022. Estimates of noble metal particle growth in a molten salt reactor. Colloids Surf. A: Physicochem. Eng. Asp. 655, 130167. http://dx.doi.org/10.1016/j.colsurfa.2022.130167.

Hewitt, D., Fornasiero, D., Ralston, J., 1995. Bubble–particle attachment. J. Chem. Soc. Faraday Trans. 91 (13), 1997–2001. http://dx.doi.org/10.1039/FT9959101997.

Huu Hoang, D., Imhof, R., Sambrook, T., Bakulin, A.E., Murzabekov, K.M., Abubakirov, B.A., Baygunakova, R.K., Rudolph, M., 2022. Recovery of fine gold loss to tailings using advanced reactor pneumatic flotation ImhoflotTM. Miner. Eng. 184, 107649. http://dx.doi.org/10.1016/j.mineng.2022.107649.

Leistner, T., Peuker, U.A., Rudolph, M., 2017. How gangue particle size can affect the recovery of ultrafine and fine particles during froth flotation. Miner. Eng. 109, 1–9. http://dx.doi.org/10.1016/j.mineng.2017.02.005.

Miettinen, T., Ralston, J., Fornasiero, D., 2010. The limits of fine particle flotation. Miner. Eng. 23 (5), 420–437. http://dx.doi.org/10.1016/j.mineng.2009.12.006.

Mohagheghian, S., Elbing, B.R., 2018. Characterization of bubble size distributions within a bubble column. Fluids 3 (1), 13. http://dx.doi.org/10.3390/fluids3010013.

Montoya, G., Lucas, D., Baglietto, E., Liao, Y., 2016. A review on mechanisms and models for the churn-turbulent flow regime. Chem. Eng. Sci. 141, 86–103. http://dx.doi.org/10.1016/j.ces.2015.09.011.

Neethling, S.J., Cilliers, J.J., 2009. The entrainment factor in froth flotation: Model for particle size and other operating parameter effects. Int. J. Miner. Process. 93 (2), 141–148. http://dx.doi.org/10.1016/j.minpro.2009.07.004.

Sarrot, V., Huang, Z., Legendre, D., Guiraud, P., 2007. Experimental determination of particles capture efficiency in flotation. Chem. Eng. Sci. 62 (24), 7359–7369. http://dx.doi.org/10.1016/j.ces.2007.08.028.

Schulze, H.J., 1989. Hydrodynamics of bubble-mineral particle collisions. Miner. Process. Extr. Met. Rev. 5 (1–4), 43–76. http://dx.doi.org/10.1080/08827508908952644.

Tao, D., 2005. Role of bubble size in flotation of coarse and fine particles—A review. Sep. Sci. Technol. 39 (4), 741–760. http://dx.doi.org/10.1081/SS-120028444.

Trahar, W.J., Warren, L.J., 1976. The flotability of very fine particles — A review. Int. J. Miner. Process. 3 (2), 103–131. http://dx.doi.org/10.1016/0301-7516(76)90029-6.

Wang, D., Liu, Q., 2021. Hydrodynamics of froth flotation and its effects on fine and ultrafine mineral particle flotation: A literature review. Miner. Eng. 173, 107220. http://dx.doi.org/10.1016/j.mineng.2021.107220.

Wang, L., Peng, Y., Runge, K., Bradshaw, D., 2015. A review of entrainment: Mechanisms, contributing factors and modelling in flotation. Miner. Eng. 70, 77–91. http://dx.doi.org/10.1016/j.mineng.2014.09.003.

Wang, P., Yvon, M., Parkes, S., Galvin, K.P., 2024a. Enhancing nickel grade and recovery with counter-current washing of the concentrated bubbly-zone of a single stage REFLUX™ flotation cell. Miner. Eng. 206, 108506. http://dx.doi.org/10.1016/j.mineng.2023.108506.

Wang, P., Yvon, M., Parkes, S., Galvin, K.P., 2024b. Improving flotation hydrodynamics to maximize nickel recovery from tailings. Miner. Eng. 216, 108880. http://dx.doi.org/10.1016/j.mineng.2024.108880.

Wiese, J., Becker, M., Yorath, G., OConnor, C., 2015. An investigation into the relationship between particle shape and entrainment. Miner. Eng. 83, 211–216. http://dx.doi.org/10.1016/j.mineng.2015.09.012.